Design of a High Force Density Tubular Motor

M. Galea, G. Buticchi, L. Empringham, L. de Lillo and C. Gerada

Abstract — This paper deals with the design, construction and experimental verification of a high force density, tubular, linear, permanent magnet motor, driven from a high power density matrix converter for an aerospace application. The work also describes the implementation and experimental verification of a novel, thermal management technique for the phase windings of electrical machines. The technique introduces a higher thermal conductivity path between the centre of the slot and the cooling arrangement, thus increasing the heat flow away from the slot centre. An introduction to the design of the motor is first given, after which an introduction to the technique is presented. A study of how the implementation of the technique affects motor performance is then presented. A detailed overview of the construction aspects is highlighted and finally, experimental validation is used to illustrate the comparison between the predicted results and the measured results, obtained from an instrumented, test rig.

Index Terms — aerospace, force density, matrix converters, more electric aircraft, thermal management, tubular motor

I. INTRODUCTION

HIGH performance electrical drive applications such as those for the aerospace industry often require the electrical machine designer to push the boundaries in terms of size, efficiency and reliability through all the design stages. The drive towards the more electric aircraft (MEA) [1, 2] seeks to reduce or remove the presence of traditional, hydraulic, pneumatic and mechanical systems from aircraft. This makes the performance of electrical machines in terms of the torque/force density, fault tolerance and reliability, doubly important [3].

Electro-mechanical actuators are today being used to provide high performance linear actuation in aircraft, however the presence of mechanical components represents a major risk in terms of reliability, which could be minimized by the elimination of screws and gear-boxes, thus pushing research towards direct drive (DD) actuation such as that achieved by linear motors. The main drawback is however the inherent

ability of linear motors to reach the required force-to-mass ratio, as expected from a mechanically-geared counterpart [4].

The objective of this paper is thus to design a tubular, linear permanent magnet (TLPM) motor and investigate ways how to improve and optimize the force and force density performance of the machine. In order to study and improve the limitations of force density synonymous with linear machine technology, a general review of recent, high force density, linear machine and methods for maximizing the force density performance of such machines is presented in [5]. The performance of any machine can be improved by addressing the two main limiting factors, namely the electro-magnetic and the thermal limit. The first is achieved by appropriate electro-magnetic design and optimization [5].

In an effort to extend the thermal limiting boundary of the machine as much as possible, a novel, thermal management technique is also introduced and investigated thoroughly in [6]. This paper will present the design and integration of the thermal management technique within a TLPM motor and will then describe the implementation and construction aspects of a prototype machine. This will be used to validate the resulting performance in an effort to quantify the benefits gained by the proposed thermal management technique.

An overview of the design of the TLPM motor is given in the next section after which an introduction to the thermal management technique is presented. Analytical and finite element (FE) models (electro-magnetic and thermal) are used to study and investigate the performance of the TLPM motor when it is implemented with the technique. The advantages gained by the implementation are compared and presented, with main focus being on the reduction of hot-spot temperatures in the windings of the machine. Experimental tests illustrate and validate the worthiness of the technique.

II. THE TLPM MOTOR

From the various, linear machine topologies that exist today [5, 7-10], in general it is the TLPM motor topology with inset permanent magnets (IPM), that offers the best force density performances [11, 12]. Considering this, then it was decided to focus the design on such an arrangement, which also has the advantage of facilitating manufacturing (in terms of the moving part, henceforth called the mover) and also reduced the amount of mover, magnetic material required.

The main design constraint for the machine described in this paper is the available external envelope. Fig. 1 shows the general structure of the double layer, 12-slot/10-pole, fluid-cooled, TLPM motor, introduced in [12] .
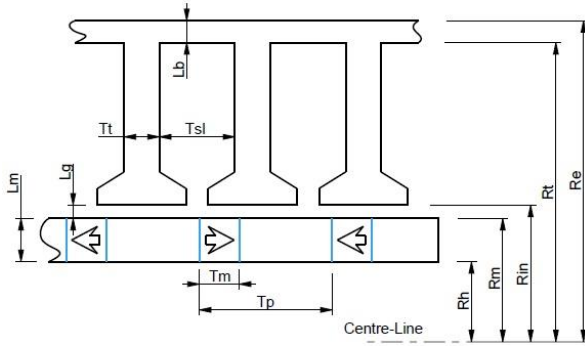
Fig. 1 Structure of the TLPM motor with IPMs

Assuming no iron losses in both stator and mover and neglecting harmonic effects due to the electrical loading, then the no load, air-gap flux density B_g can be described by (1), where B_{rem} is the PM residual flux density, $T_c = (T_p - T_m)$ and μ_{rrec} is the PM relative recoil permeability.

$$B_g = B_{rem} \times \frac{\frac{T_m}{\mu_{rrec}}[R_m^2 - R_h^2]}{L_g[R_m^2 - R_h^2] + \left(\frac{T_m}{\mu_{rrec}}\right)\left(\frac{T_c}{4}\right)(R_{in} + R_m)} \quad (1)$$

The electrical loading A_{rms} is dependent on the thermal management and material properties of the machine. Assuming that the only source of heat is the I^2R loss and that the predominant thermal dissipation in the machine is in the radial direction, then one slot pitch of the double layer, TLPM motor can be modeled as shown in Fig. 2. The thermal resistances R_1 - R_{12} are given in [6, 12], while R_{wat}, R_{hc} and R_{tipa} are defining radii for the thermal calculations. Capacitors representing thermal masses can be easily added if transient behavior needs to be evaluated.
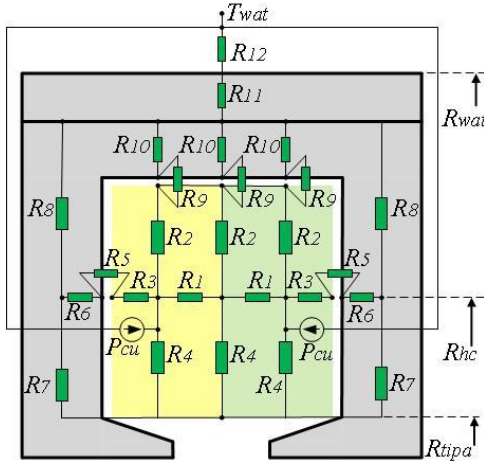

Fig. 2 Lumped parameter thermal network

The thermal/electrical limits can be computed using the thermal network, shown in Fig. 2. Having a maximum permissible winding temperature T_{max}, the maximum value of copper losses P_{cu} for each coil can be found. The maximum value of the copper current density J_{rms} (and thus A_{rms}) can be found from (2), where ρ_{cu} is the resistivity of copper at a given winding temperature and K_{fill} is the slot fill factor.

$$P_{cu} = \pi \times T_{sl}R_{hc}K_{fill} \times \rho_{cu}(R_t - R_{tipa})J_{rms}^2 \quad (2)$$

The peak thrust force F_{lin} generated by the machine can then be computed from (3) where B_{g1} is the fundamental component of the air-gap flux density distribution, P is the number of pole pairs and $(4\pi R_{in}PT_p)$ is the total active surface area of the mover.

$$F_{lin} = B_{g1} \times \left(\sqrt{2} \times A_{rms}\right) \times 4\pi R_{in}PT_p \quad (3)$$

$$B_{g1} = \frac{4}{\pi}B_g \sin\left(\frac{\pi(T_p - T_m)}{2T_p}\right) \quad (4)$$

Using the above, the optimum split ratio and tooth width to slot width ratio for maximum force can be found. The design is initiated by considering any fixed parameters such as the external length L_e, external radius R_e and B_{rem} and μ_{rrec}. Then using (1) – (4), the optimum geometrical dimensions can be found. The analytical models above are used to provide adequate starting points for a more accurate FE model, such as shown in Fig. 3. The thermal limit in the windings T_{max} is set to $180°C$. The thermal model shown in Fig. 2 is used to identify the maximum peak current density J_{pk} that satisfies the required thermal limit. A FE model, such as shown in Fig. 3 is then used to evaluate the performance of the TLPM motor at this value of current loading.
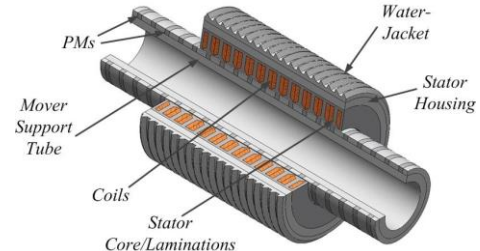

Fig. 3 The TLPM motor

III. THE THERMAL MANAGEMENT TECHNIQUE

In general all electrical machines are subject to the constraints imposed by the materials (copper, insulation, soft and hard magnetic materials) from which their main components are constructed [13]. These constraints can be considered to fall into two main categories, namely the electro-magnetic and the thermal limit. These two limits quantify what force/torque can be obtained from a particular machine. In Section II, the main focus is on the optimization of the electro-magnetic limit (and how to maximize it), however extending the thermal limit by adequate thermal management structures can automatically result in machines that can operate at higher current loading, thus achieving a higher torque/force for the same machine mass. For a fluid-cooled machine such as that shown in Fig. 3, this can be achieved by introducing a low thermal resistance path between the winding hot-spots and the cooling arrangement [6].

Fig. 4a shows one slot of the TLPM motor where the various materials (hence the various thermal resistances) that make up this area can be observed. As illustrated in the

representative thermal resistance network of Fig. 4b, where R_{pot}, R_{ins} and R_{liner} represent the thermal resistance of the potting compound, the copper insulation and the slot liner respectively, the total effective thermal resistance to the conductors' P_{cu} can be quite significant.

a) TLPM motor slot
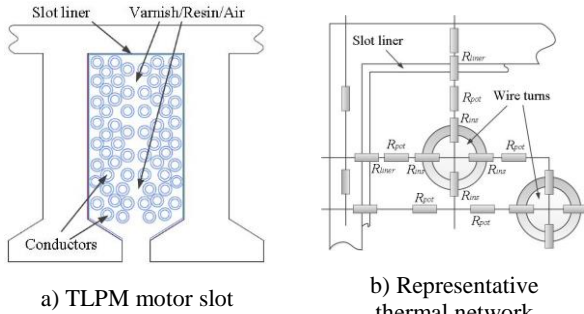
b) Representative thermal network

Fig. 4 The TLPM motor slot area

However, by inserting a heat flow path (HP) such as shown in Fig. 5a, the thermal resistance of the dominant heat conduction path is reduced. This achieves an enhanced equivalent thermal conductivity k_{eq} from the center of the slot towards the outer walls, which should result in a better distribution of heat over the slot area and also in an overall reduction of peak hot-spot temperature. The negative implications of introducing this path, whose structural definitions are shown in Fig. 5b, are the smaller winding area, higher P_{cu} for the same A_{rms} and any additional eddy losses P_{ed_HP} in the HP itself. The material to be used for the HP needs to have a high thermal conductivity and a low effective electrical conductivity, which can be achieved through segmentation.
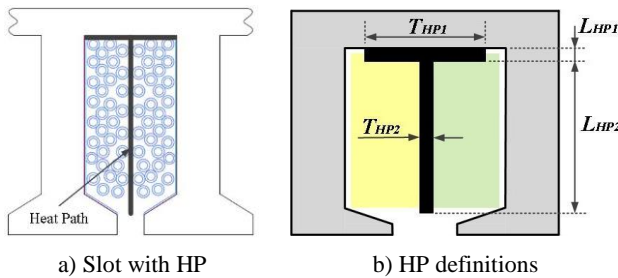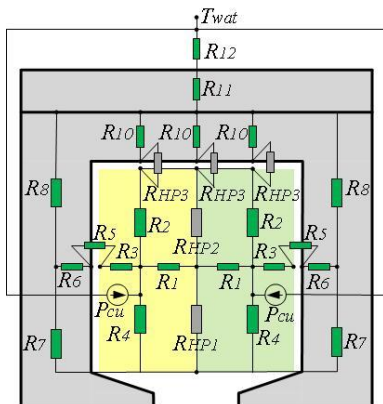

a) Slot with HP

b) HP definitions

Fig. 5 The HP

Fig. 6 Lumped parameter thermal network with HP

As the thermal improvement technique involves the insertion of a piece of thermal conductive material as shown in Fig. 5 into the slot, then the resulting lumped parameter network is as shown in Fig. 6, where it can be seen that R_{HP1}, R_{HP2} and R_{HP3} represent the HP itself. The derivations of the thermal resistances are given in [6, 12].

IV. IMPLEMENTATION OF THE TECHNIQUE

The concept and the analytical/simulation validation of the thermal management technique are presented in this section, where a brief overview on the design and implementation of the technique is presented.

A. Initial verification

Initial verification tests to confirm the general effectiveness of the technique are done. The two models of Fig. 2 and Fig. 6 are tested by considering the total copper loss P_{cu_tot} of the TLPM motor at steady state for a constant F_{lin} (i.e. equal linear A_{rms} and J_{pk}). Fig. 7 compares the results, where it is immediately clear that with the HP, the peak hot-spot temperature in the winding has decreased considerably ($\approx 110°C$ compared to $\approx 180°C$) thus confirming the effectiveness of the technique.

Fig. 7 also compares the peak temperatures from the lumped parameter network models with results from thermal FE models. An electro-magnetic/thermal FE software package is used to model the slot of the TLPM motor with and without the HP and simulated with the same conditions assumed for the lumped parameter models. The results from both models show a reasonable similarity, thus validating the analytical models while again confirming the benefits of the HP in the slot.
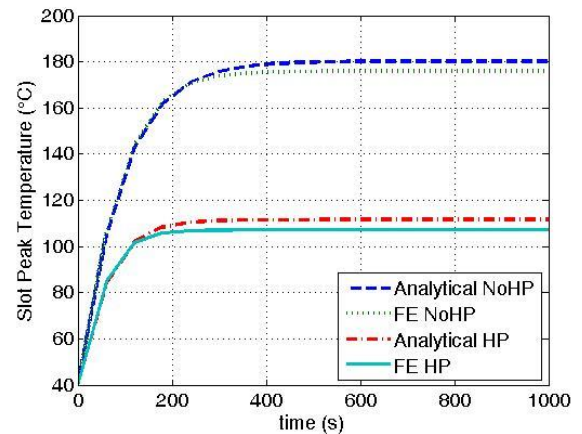

Fig. 7 Comparing analytical with FE results

B. Design and optimization

The thermal FE and lumped parameter models are then used to investigate the various designs of the shape and thickness of the HP in order to identify the optimal geometry.

From Fig. 5a, it can be visually deduced that it is the HP thickness T_{HP2} that has the main effect on the thermal performance of the arrangement. In general the thicker is the HP the lower is its thermal resistance, however a thicker HP takes up more space, thus increasing P_{cu}. An optimum value

exists and is selected by testing the FE model for various values of T_{HP2}, where for each test J_{pk} is adjusted to achieve a T_{max} of $180°C$. Fig. 8 plots the motor F_{lin} and P_{cu_tot} for increasing values of T_{HP2} (for a constant T_{sl}).
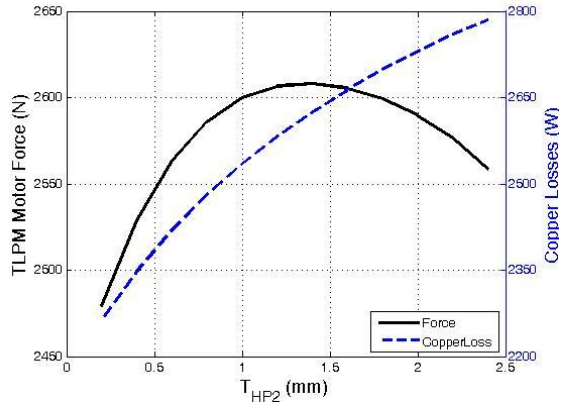

Fig. 8 Optimization of T_{HP2}

From Fig. 8, it can be observed how an optimal value of T_{HP2} exists. The generated F_{lin} is increasing, because the thicker HP permits higher current loadings, but beyond the optimal value, the increasing P_{cu_tot} due to the reducing copper area results in a reduction in the J_{pk} allowed by the T_{max} constraint and F_{lin} starts decreasing again. An important feature of T_{HP2} is its relationship with T_{sl}., i.e. the optimal T_{HP2} that results in the maximum J_{pk} allowed by T_{max}. This is investigated thoroughly in [6], where it was observed how for relatively small slot width values, the optimal T_{HP2} exhibits a linear increase relative to T_{sl}. As T_{sl} increases (for the same slot height) the relative impact of the HP decreases and the radial heat transfer path through the conductors and resin to the back iron becomes more dominant.

Considering Fig. 5, it can be observed that the optimization of the HP length L_{HP2} resides in the fact that it need only be long enough to 'thermally short-circuit' the hot-spot point to the stator back iron at R_t. In practice, this can be achieved by using the whole depth of the slot ($L_{HP2} = R_t - R_{in}$) as a smaller length will not result in any practical advantage because the pre-formed coil window will still have the same dimensions.

Theoretically, the thickness L_{HP1} and the span T_{HP1} do not have any significant effect on the reduction of the dominant thermal resistance of the slot. But practical values for T_{HP1} and L_{HP1} still need to be set with the main objective being to achieve maximum contact between the surface of the HP and the slot walls whilst keeping the material volume to a minimum.

In terms of P_{ed_HP}, the phenomenon can be virtually eliminated by employing a combination of slits and slots in the HP, as illustrated in Fig. 9. Fig. 10 compares the P_{ed_HP} for the proposed HPs at $50Hz$, showing the effectiveness of the slitting method to reduce the flow of eddy currents. A combination of one complete slit as shown in Fig. 9a and two non-complete slits (Fig. 9b) is therefore suggested, resulting in good mechanical robustness, minimum interference with the thermal behavior of the HP and low P_{ed_HP}.

a) HP1: Solid   b) HP2: Slit   a) HP3: Partial Slit
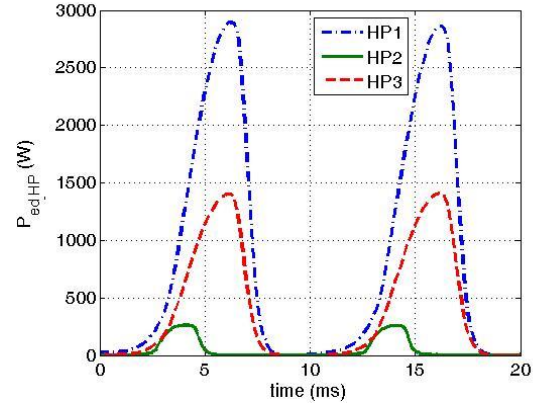Fig. 9 Proposed HPs for P_{ed_HP} reduction

Fig. 10 Minimization of P_{ed_HP} via slitting

C. Implementation onto the TLPM motor

In this section, the technique is implemented onto the TLPM motor of Section II. Using the optimization procedures mentioned above, an optimal shape, geometry and composition for the HP is found. The FE model of Fig. 3 is then equipped with such a HP and this is represented in Fig. 11. Keeping the same thermal limit T_{max} as before, then the thermal model of Fig. 6 (with HP) is used to identify the maximum J_{pk} that satisfies the required thermal limit. The FE model, represented by Fig. 11 is then used to evaluate the performance of the TLPM motor at this value of J_{pk}.
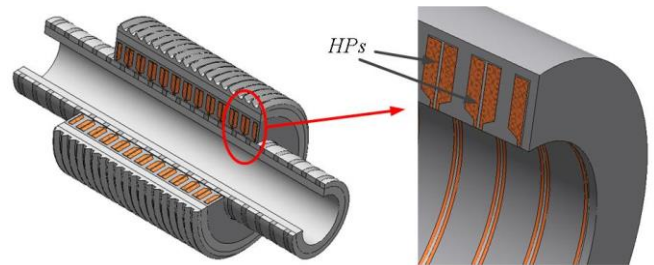

Fig. 11 The TLPM motor with HPs

D. Results and comparisons

The performance of the TLPM motor without the HP ($J_{pk} = 16A/mm^2$ as found from Fig. 2) is then compared with the results of when the HP is implemented ($J_{pk} = 25A/mm^2$ as found from Fig. 6). The force capability of the two models is compared in Fig. 12, where the higher electric loading capability due to the insertion of the HP can be easily observed. Fig. 12 shows a slightly lower force capability for the HP model (for the same J_{pk}) which is mainly due to the effect of reduced effective current loading for the same J_{pk}. Fig. 12 also illustrates the different operating points of the

machine (according to the thermal limitation of T_{max}). As explained previously, when the HP is implemented, the TLPM motor operates safely at a $J_{pk} = 25A/mm^2$ which results in a higher generated force. The force density capability of the two models (considering active and inactive components) is illustrated in Fig. 13, which shows the reduced performance (at the same J_{pk}) due to the space taken by the HP.
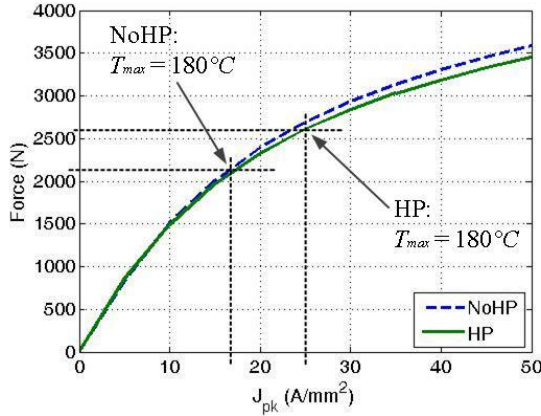

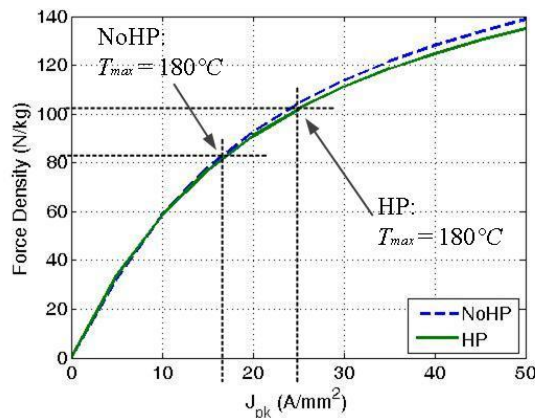Fig. 12 HP vs. NoHP comparisons: force capability

Fig. 13 HP vs. NoHP comparisons: force density

The overall performance parameters of the TLPM motor, with and without the HP is presented in Table I, where T_{wat} is the temperature of the cooling fluid, δ_g is the air-gap shear stress and the main constraint for a fair comparison is the thermal limit set by T_{max}. Table I clearly illustrates the advantages in terms of current loading and air-gap shear stress gained by the implementation of the thermal management technique for the TLPM motor.

TABLE I
TLPM MOTOR PARAMETERS WITH AND WITHOUT THE HP

	No HP	**HP**
J_{pk} (**A/mm²**)	16	25
A_{rms} (**kA/m**)	85.83	117.82
P_{cu_tot} (**kW**)	1.3	2.78
δ_g (**kN/m²**)	35.3	43.96
T_{max} (**°C**)	180	180
T_{wat} (**°C**)	40	40

V. PM DEMAGNETIZATION RISK ANALYSIS

Considering the high, operating conditions of the motor (a continuous J_{pk} of $25A/mm^2$ when the HP is implemented, resulting in a winding $T_{max} \approx 180°C$) an investigation into the behavior and the merits and demerits of the IPM configuration used is initiated. The main point of interest of this part of the analysis process is the potential risk of irreversible demagnetization of the permanent magnets. The permanent magnet (PM) material chosen for the TLPM motor is an N40 grade of Neodymium Iron Boron (NdFeB), whose demagnetization curves are shown in Fig. 14.
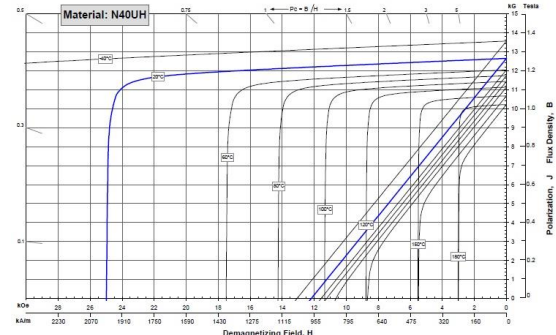

Fig. 14 N40UH demagnetization curves

Irreversible demagnetization occurs when the PM operating point goes below the knee value of the closed loop curves shown in Fig. 14. As the operating PM temperature T_{pm} increases, this knee-limit in terms of B increases, in fact for a worst case operating T_{pm} of 180°C, it is approximately situated at 0.8T. This means that at 180°C, if the flux density field B in the direction of the PM magnetization goes below 0.8T, then irreversible demagnetization occurs. The demagnetisation analysis is performed by setting a demagnetisation proximity field B_{prox} as described in (5), where B_{demag} is the PM material demagnetisation value (i.e. the knee point), $\underline{M}$ is a magnetisation vector indicating the direction of magnetisation and M is the norm of the vector $\underline{M}$.

$$B_{prox} = B_{demag} - \underline{B} \cdot \frac{\underline{M}}{M} \qquad (5)$$

From (5), a reliable demagnetisation prediction technique can be achieved. If $B_{prox} \leq 0$, then there is no risk of demagnetisation while if $B_{prox} > 0$ then there is a risk of potential demagnetisation. It can be perceived from (5), that the more positive B_{prox} is, then the more important (irreversible) the demagnetisation is. Using (5) in conjunction with a FE analysis, the demagnetization prediction for the worst case T_{pm} of 180°C, both at no load and peak load can be obtained. This is shown in Fig. 15, where the color red is used to show complete demagnetization. From Fig. 15, it can be observed how even for a worst case PM temperature, only a small, negligible amount of irreversible demagnetization occurs for the peak load condition. This means that if during peak load conditions, the mover of the machine ever operates at temperatures of 180°C, then a small amount of material (less than 0.5% for each individual PM) would be lost. However it is important to note that the T_{max} quoted throughout this paper is in general assumed to be in the windings which automatically indicates that the mover temperature is considerably lower.
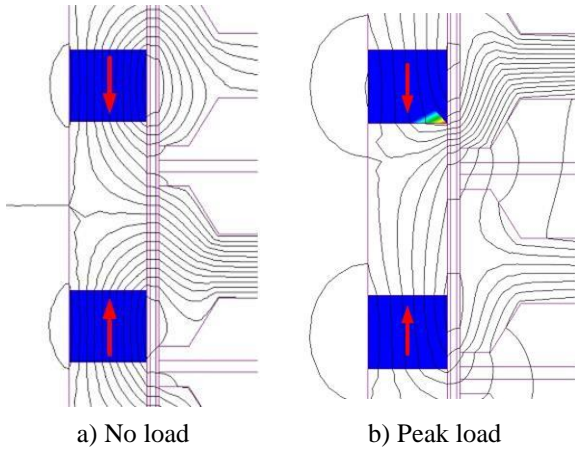
a) No load   b) Peak load

Fig. 15 Demagnetization prediction at $T_{pm} = 180°C$

VI. MANUFACTURING OF THE TLPM MOTOR

A prototype machine is built and tested. The construction, assembly and general manufacturing of the machine are presented in this section. Traditionally the nature of tubular motors results in their manufacturing and construction to be very difficult and somewhat expensive.

A. The coils

The nature of the TLPM motor dictates that the coils be pre-manufactured. The toroid shape of the coils permits the coils to be wound individually (under tension to increase the slot fill factor K_{fill}). This can be achieved by manufacturing a specific coil former and then winding the coil directly on it.

Considering the high thermal performance that is required from the motor, it was decided to impregnate the wound coils with a high thermally conductive potting compound. Fig. 16a shows an exploded view of the coil former assembly and Fig. 16b shows a cross-sectional view of the assembled former. From Fig. 16b it can be perceived, how the coil is first wound, then impregnated via the holes bored on purpose to inject the compound (in its liquid form) and then cured at room temperature or in an oven. When cured, the former is taken apart and a coil, such as shown in Fig. 17b is produced.
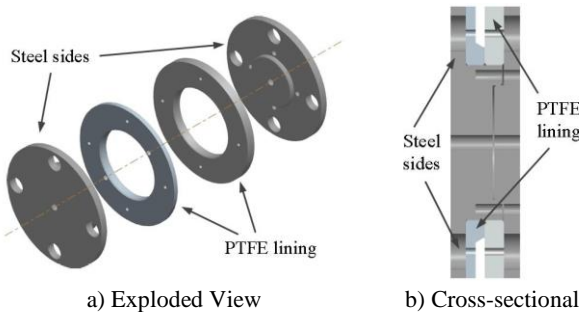

a) Exploded View   b) Cross-sectional

Fig. 16 The coil former assembly

B. The stator assembly

The most challenging part of the construction of the TLPM motor is represented by the construction and assembly of the stator. While the nature of rotational machines and even that

of standard, linear machines makes the implementation of the stator laminations a relatively easy task, in the case of a tubular motor the building and attaching of the axial stator laminations is much more complicated and requires careful manufacturing and assembly planning.

An innovative methodology where the stator is built up in a succession of 'stator rings' as shown in Fig. 17c is used. These stator 'rings' and the HPs of Fig. 17a are assembled in a similar manner to the 'exploded' view shown in Fig. 17d, which stresses the importance of having good contact between all the surfaces for thermal purposes. The complete re-assembled stator housing with all the coils and HPs inside as shown in Fig. 17e, is then fit (with a positive interference) into a pre-manufactured stator water-jacket, whose material is aluminum. The final stator assembly is illustrated in Fig. 17f.

a) HP   b) Pre-formed coils

c) Assembly structure   d) Exploded view

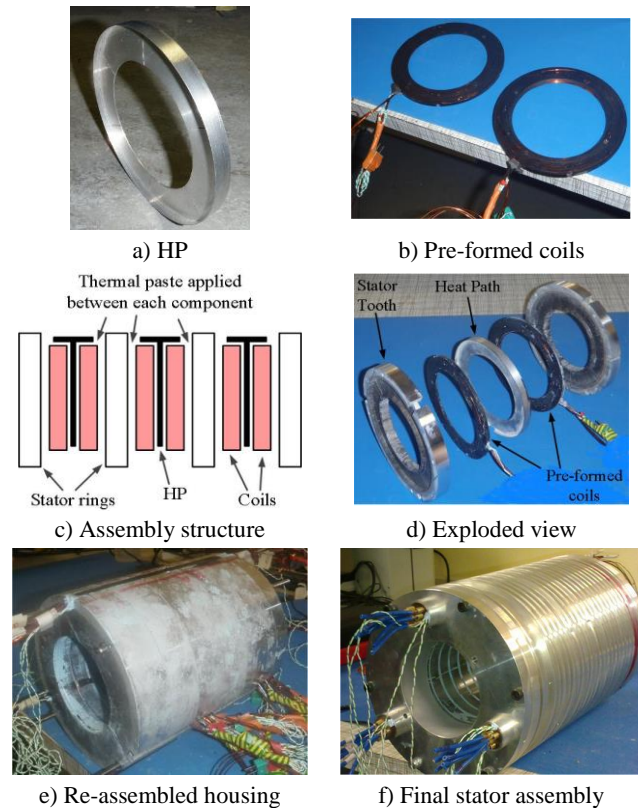e) Re-assembled housing   f) Final stator assembly

Fig. 17 Stator assembly components

C. The mover assembly

For an IPM configuration such as shown in Fig. 1, the mover consists of the axially magnetized PMs, the ferromagnetic, flux-focusing pieces and the non-ferromagnetic support tube. Fig. 18 illustrates the complete mover assembly including the force transmission shafts.
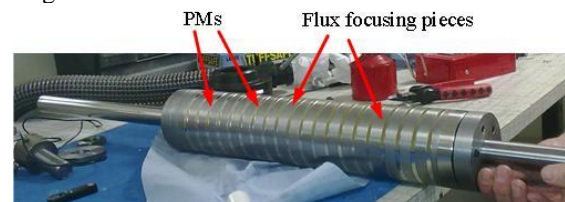

Fig. 18 The mover assembly

D. General assembly and the test-rig

A cross-sectional view of the motor assembly is shown in Fig. 19, where the various components mentioned above can be observed.
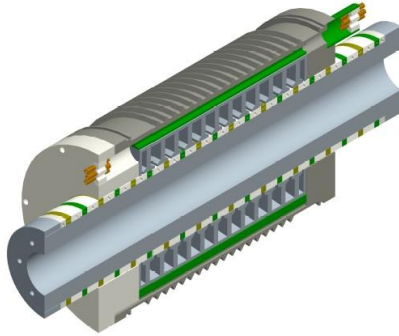

Fig. 19 The motor assembly

The whole motor is assembled on a test-bed that includes linear bearing guides, support plates and a load actuator for testing purposes. The complete test-rig is shown in Fig. 20. The load actuator is an industrial, $40kW$ EMA, capable of peak force loads up to $17.8kN$ with a maximum stroke of $300mm$ at a maximum linear velocity of $313mm/s$. These performance parameters ensure that a complete set of tests can be done for the TLPM motor. A high performance, water-cooled, $100kW$, matrix converter [14] is used to drive the TLPM motor. A linear force cell with an accuracy of 1% of the full scale measurement of $10kN$ is used for linear force measurements.
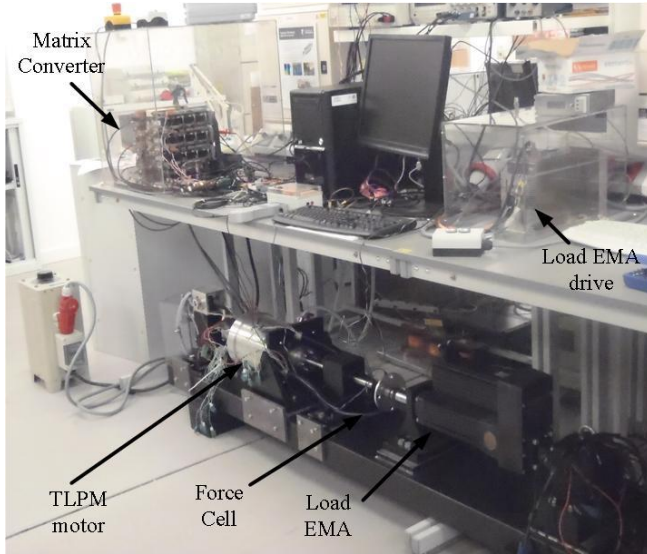

Fig. 20 The complete test-rig

VII. Experimental Validation

A series of tests are done on the experimental rig of Fig. 20, in order to validate the TLPM motor performance when it is equipped with the HP technique and thus compare the experimental results to the modeling results.

A. Measurable parameters of the TLPM motor

Having the assembled motor and rig permits the measurement of certain parameters that are critical to the operation of the machine. Table II compares the predicted and measured values (at a reference temperature T_{wat} of $40°C$) of the phase resistance R_a and the phase inductance L_a, where the prediction errors can be attributed to manufacturing tolerance, extra internal connection leads and variations in the soft magnetic material properties.

TABLE II
COMPARISON OF MEASURABLE PARAMETERS

	FE	Experimental
R_a (Ω)	0.5103	0.59
L_a (mH)	10.6	10

B. Slot temperature distribution

As shown in Fig. 17e and Fig. 17f, the TLPM motor is equipped with a number of thermocouples so as to be able to monitor and record the operating temperatures in various parts of the machine. Each coil in the machine has a thermocouple that is placed in the same location as the point C_{2_HP} of Fig. 21 below. However, three slots (one per phase) have the full distributed thermocouple array shown in Fig. 21.
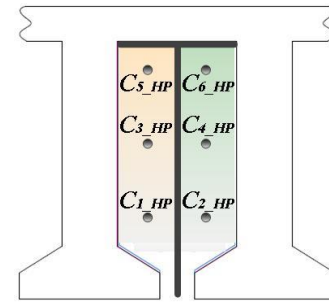

Fig. 21 Temperature monitoring array

The temperature distribution in the slot during the full load operation of the TLPM motor (at $J_{pk} = 25A/mm^2$) is measured by monitoring one of these fully instrumented slots. These tests are done with an initial $T_{wat} = 40°C$ and the velocity of the cooling fluid $V_{wat} = 1m/s$. Fig. 22 compares the measured temperatures of the points C_{2_HP}, C_{4_HP} and C_{6_HP} with the FE-predicted results for the same load conditions. For reasons of clarity and visualization, only these three points are illustrated in Fig. 22, with similar results being obtained for the other three points.

It is immediately clear that very good similarity is achieved between the predicted and measured results. As can be observed from Fig. 22, at full load, the experimentally measured, maximum hot-spot temperature (C_{2_HP}) settles to a temperature of approximately $190°C$. Considering that the copper used for the motor windings has an insulation class that is rated at $220°C$ and the thermal paste used for potting is also rated at $220°C$, then this can be considered as a safe temperature even if it slightly exceeds the set T_{max}. Further reduction in temperature can be achieved simply by increasing V_{wat} or decreasing T_{wat}.

This article has been accepted for publication in a future issue of this journal, but has not been fully edited. Content may change prior to final publication. Citation information: DOI 10.1109/TIA.2014.2300190, IEEE Transactions on Industry Applications

> REPLACE THIS LINE WITH YOUR PAPER IDENTIFICATION NUMBER (DOUBLE-CLICK HERE TO EDIT) <   8
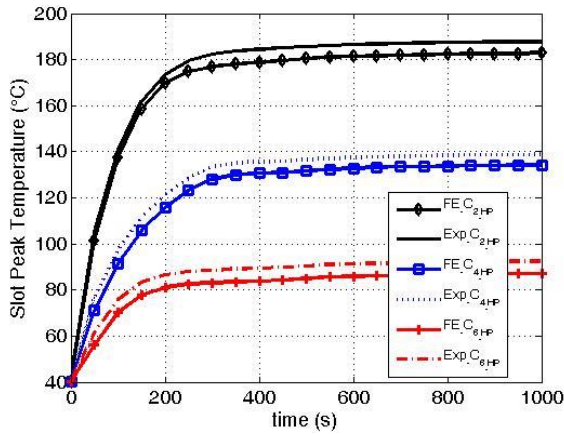
Fig. 22 Comparison of slot temperature distribution

C. Force capability of the TLPM motor

To measure the force capability of the TLPM motor, a suitable control strategy making use of a precise position loop, is designed and implemented in the matrix converter controller. The load EMA is controlled via current loop control to maintain a specific load. The linear force cell shown in Fig. 20 is used to obtain values of the linear force generated. The tests are done for increasing values of the peak phase current I_{pk}. Fig. 23 shows the experimental results and also compares them to the FE-predicted ones.
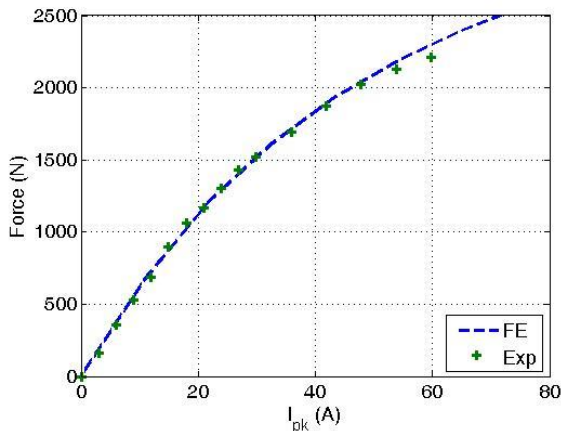

Fig. 23 Comparison of TLPM motor force capability

As can be observed from Fig. 23, a very good similarity exists between the predicted results and the measured results, thus validating the design procedures and the FE model of Fig. 11. Any remaining prediction errors can be attributed to inaccuracies in measurement due to the load cell tolerance, human error and manufacturing and material tolerances.

VIII. CONCLUSION

Considering the nature and the design requirements of the TLPM motor, then from the above the most critical output parameter of the motor is of course its force capability and its ability to withstand the requirement both thermally and electro-magnetically. The capability of the machine to satisfy the requirements from both perspectives can easily be observed in Fig. 22 and Fig. 23.

The experimentally measured, performance capability of the TLPM motor is presented and compared to the predicted capability in tabulated form in Table III.

The results are shown for the rated condition of $J_{pk} = 25A/mm^2$, where the force density is calculated assuming the presence of both active and non-active components of the TLPM motor.

The performance chart shown below clearly illustrates the similarities between the models' and the prototype's results, while also highlights the excellent force density performance achieved. The results achieved by the TLPM motor presented in this paper, compare excellently with results published in available literature [9, 11, 15, 16] concerning high force density, linear machines.

TABLE III
FINAL PERFORMANCE CHART OF THE TLPM MOTOR

	Predicted	Experimental
R_a (Ω)	0.5103	0.59
L_a (mH)	10.6	10
J_{pk} (A/mm^2)	25	25
T_{max} $(°C)$	180	188.89
Force density (kN/m^3)	383.2	381.42

The excellent values of force density are partly dependent on the implementation of the thermal management technique, which was successfully implemented to the TLPM motor in this work. As can be observed from Fig. 13, the insertion of the HP into the slot has resulted in an increase of copper current density of approximately 20.53% and a corresponding force density increase of approximately 20%, while still respecting the thermal limit set by $T_{max} = 180°C$. This results in considerable improvement in the force capability of the machine. Overall the results presented in this paper, validate and justify the implementation of the thermal management technique.

REFERENCES

[1] A. Boglietti, A. Cavagnino, A. Tenconi, and S. Vaschetto, "The safety critical electric machines and drives in the more electric aircraft: A survey," in *Industrial Electronics, 2009. IECON '09. 35th Annual Conference of IEEE*, 2009, pp. 2587-2594.

[2] R. I. Jones, "The More Electric Aircraft: the past and the future?," in *Electrical Machines and Systems for the More Electric Aircraft (Ref. No. 1999/180), IEE Colloquium on*, 1999, pp. 1/1-1/4.

[3] T. Raminosoa, C. Gerada, and M. Galea, "Design Considerations for a Fault-Tolerant Flux-Switching Permanent-Magnet Machine," *Industrial Electronics, IEEE Transactions on,* vol. 58, pp. 2818-2825, 2011.

[4] G. W. McLean, "Review of recent progress in linear motors," *Electric Power Applications, IEE Proceedings B,* vol. 135, pp. 380-416, 1988.

[5] M. Galea, C. Gerada, T. Raminosoa, and P. W. Wheeler, "Considerations for the design of a tubular motor for an aerospace application," in *Electrical Machines and Systems (ICEMS), 2011 International Conference on*, 2011, pp. 1-6.

[6] M. Galea, C. Gerada, T. Raminosoa, and P. Wheeler, "A Thermal Improvement Technique for the Phase Windings of Electrical Machines," *Industry Applications, IEEE Transactions on,* vol. 48, pp. 79-87, 2012.

[7]   J. Wang, G. W. Jewell, and D. Howe, "Design optimisation and comparison of tubular permanent magnet machine topologies," *Electric Power Applications, IEE Proceedings -,* vol. 148, pp. 456-464, 2001.

[8]   J. F. Gieras and Z. J. Piech, *Linear Synchronous Motors: Transportation and Automation Systems*: CRC Press LLC, 2000.

[9]   N. Ziegler, D. Matt, J. Jac, T. Martire, and P. Enrici, "High force linear actuator for an aeronautical application. Association with a fault tolerant converter," in *Electrical Machines and Power Electronics, 2007. ACEMP '07. International Aegean Conference on,* 2007, pp. 76-80.

[10]   P. E. Cavarec, H. Ben Ahmed, and B. Multon, "Force density improvements from increasing the number of airgap surfaces in synchronous linear actuators," *Electric Power Applications, IEE Proceedings -,* vol. 150, pp. 106-116, 2003.

[11]   N. Bianchi, S. Bolognani, D. D. Corte, and F. Tonel, "Tubular linear permanent magnet motors: an overall comparison," *Industry Applications, IEEE Transactions on,* vol. 39, pp. 466-475, 2003.

[12]   M. Galea, "High Performance, Direct Drive Machines for Aerospace Applications," PhD, Faculty of Engineering, University of Nottingham, UK, 2013.

[13]   A. Hughes, *Electric motors and drives: fundumentals, types and applications*, 3rd ed. Oxford: Newnes, 2006.

[14]   L. Empringham, P. Wheeler, and J. Clare, "Power density improvement and robust commutation for a 100 kW Si-SiC matrix converter," in *Power Electronics and Applications, 2009. EPE '09. 13th European Conference on*, 2009, pp. 1-8.

[15]   W. Jiabin, W. Weiya, and K. Atallah, "A Linear Permanent-Magnet Motor for Active Vehicle Suspension," *Vehicular Technology, IEEE Transactions on,* vol. 60, pp. 55-63, 2011.

[16]   D. M. Joseph and W. A. Cronje, "Design and Analysis of a Double-Sided Tubular Linear Synchronous Generator with Particular Application to Wave-Energy Conversion," in *Power Engineering Society Conference and Exposition in Africa, 2007. PowerAfrica '07. IEEE*, 2007, pp. 1-8.
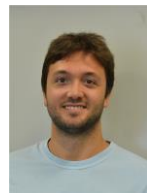
Giampaolo Buticchi (S'10-M'13) was born in Parma, Italy, in 1985. He received the Masters degree in Electronic Engineering in 2009 and the Ph.D degree in Information Technologies in 2013 from the University of Parma, Italy. He is now working as a postdoctoral research associate in the same university. His research area is focused on power electronics for renewable energy systems, static energy conversion and motor drives**.**

Lee Empringham (M'10) received a B.Eng (hons) degree in Electrical and Electronic Engineering from the University of Nottingham, UK in 1996. He then joined the Power Electronics, Machines and Control Group within the School of Electrical and Electronic Engineering at the University of Nottingham, UK to work on matrix converter commutation techniques. He received his PhD degree in November 2000. Since then he has been employed by the group as a research fellow to support different ongoing matrix converter projects and has recently been appointed to the position of Principal Research Fellow. His research interests include Direct AC-AC power conversion, Variable Speed AC Motor Drives using different circuit topologies and More-Electric / Electric Aircraft applications. Dr Lee Empringham is a member of the Institution of Electrical Engineers and the Institute of Electrical and Electronic Engineers.

Liliana de Lillo (M'09) received an M.Eng Degree in Electronic Engineering from Politecnico di Bari, Italy in 2001. She joined the Power Electronics, Machines and control group at the University of Nottingham and received a PhD degree in Electrical Engineering in 2006. She now works within the group as a Senior Research Fellow with interests in Direct AC-AC converters, Fault tolerant systems, More Electric Aircraft applications and AC Drives.

Michael Galea received his PhD in electrical machines design from the University of Nottingham, UK in 2013. He is currently working as a Research Fellow within the Power Electronics, Machines and Control Group at the University of Nottingham, UK. His main research interests are design of electrical drives, design and analysis of electrical machines and thermal management of electrical drives.

Chris Gerada (M'05) obtained his PhD in Numerical Modelling of Electrical Machines from the University of Nottingham, UK in 2005. He subsequently worked as a researcher at the University of Nottingham on high performance electrical drives and on the design and modelling of electromagnetic actuators for aerospace applications. He was appointed as Lecturer in Electrical Machines in 2008, an Associate Professor in 2011 and Professor in 2013. His core research interests include the design and modelling of high performance electric drives and machines. Prof. Gerada has been the project manager of the GE Aviation Strategic Partnership since 2006 and in 2011 was awarded a Royal Academy of Engineering Senior Research Fellowship supported by Cummins. He is also an Associate Editor for the Transactions in Industry Applications and executive member of the management board of the UK Magnetic Society and the IET Aerospace Technical and Professional Network.